ACS OMEGA

Open Access

http://pubs.acs.org/journal/acsodf

Article

Preparation of Thin-Layered Hexagonal Boron Nitride Nanosheet with Oxygen Doping

Wenqian Li, Lijun Jiang,* Wenquan Jiang,* Yuanfang Wu, Xiumei Guo, Zhinian Li, Huiping Yuan, and Man Luo

Cite This: *ACS Omega* 2024, 9, 37572−37584

Read Online

ACCESS | Metrics & More | Article Recommendations | Supporting Information

ABSTRACT: Hexagonal boron nitride nanosheet (h-BNNS), a structural analogue of graphene, possesses remarkable properties such as exceptional electrical insulation, great resistance to corrosion, excellent mechanical strength, and thermal conductivity. Nonetheless, its continued development is still hampered by the lack of a preparation technique with an easy-to-follow procedure and reliable composition and structure control. In this study, we investigated a two-step protocol for uniform size production of thin-layered h-BNNS. By carefully manipulating the crystallization degree during synthesis of h-BN powder and employing subsequent hydrothermal treatment, we successfully obtained h-BNNS with an even thickness of only a few atomic layers. Compared with the broadly used liquid-phase exfoliation process, not only is the thickness significantly decreased but also the yield is considerably elevated to several grams. Moreover, the in-plane O doping content can be adjusted within a relatively wide range. Overall, our finding demonstrates the potential of this approach in facilitating the exploration and utilization of h-BNNS.

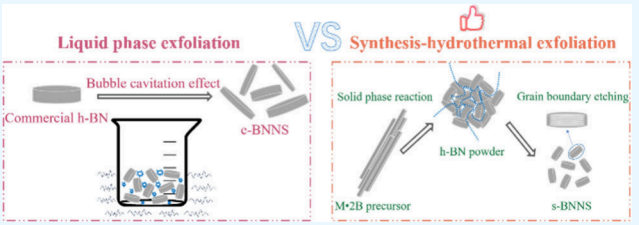

1. INTRODUCTION

A range of advanced two-dimensional (2D) materials have attracted lots of attention in recent years because of appealing performance in numerous applications.[1−3] Usually, a "nanosheet" refers to the 2D materials which possess thickness in the *c*-axis direction of less than 5 nm. This kind of structure produces a very substantial specific surface area, and it can conveniently form into thin films or dispersions in various liquids, demonstrating common practicality.[4] Additionally, the nano size distribution brings about an intriguing quantum tunneling effect that affects the chemical and physical characteristics.[5] h-BNNS is a particular kind of 2D material. In addition to the above qualities, it also possesses excellent thermal conductivity, good electrical insulation, outstanding mechanical strength, and superior chemical stability.[6−8] For example, the elastic modulus of single-layer h-BNNS was measured to be 0.865 TPa and its mechanical strength shows no reduction with increasing thickness, making it one of the strongest electrically insulating materials.[6] Besides, it was calculated that the high-quality single layer h-BNNS has a thermal conductivity of 751 W/mK at room temperature, being the second largest per unit weight among all semiconductors and insulators.[7] In other research, the horizontal and inclined self-assembly of 2D h-BNNS exhibits an unprecedented fast and selective transport performance with ethylene as well as remarkably improved long-term stability for 180 h. This even outperformed common gas separation membranes and displayed a wide range of applications in the petrochemical field.[9] Thanks to these advantages, it can be used in many different industries, such as mechanical reinforcement, electronic encapsulation, corrosion resistance, thermally enhanced filling, catalyst carriers, etc.[10]

Currently, there have been many optimistic theoretical predictions about h-BNNS, but progress in relevant experimental studies has been hindered due to the difficulty of its preparation. This gap describes the importance of exploration of the preparation methods, which can achieve a desirable balance between operational feasibility, economic cost, crystal structure, and chemical composition control. It is well-known that there are two categories of tactics to prepare h-BNNS material.[11] The "bottom to top" approach represents chemical synthesis using B- and N-containing ingredients. The usual methods are chemical or physical evaporation depositions, both of which need highly specialized equipment and intricate product separation procedurs.[12] Even though they are capable of generating nanosheets with micrometer-scale lateral size and a fine degree of crystallization, impurity inducement from catalyst or byproduct still remains as an obstacle.[13] Another representative method is chemical-blowing synthesis.[14] It

Received: January 30, 2024
Revised: June 17, 2024
Accepted: August 14, 2024
Published: August 28, 2024

makes use of gases produced by C, O, S, and H components in the raw substance, which enable the solid skeleton to burst into massive bubbles. Following dissipation of the gases and completion of the reaction, the bubble wall framework can thus transform into thin h-BNNS. However, the ultimate outgrowth usually comes in as polycrystalline pellets, which demands additional treatment. On the other hand there is a "top to bottom" strategy, meaning exfoliation of bulk h-BN powder. Yet, the interaction between adjacent layers of h-BN is hard to overcome. This is caused by a "lip-lip" interaction which is distinct from and increasingly difficult in comparison to the preparation of graphene.[15] Thus, it takes a long period of time to acquire a high productivity through common exfoliation with assistance of ultrasonic vibration, fluid shearing force, or mechanical peeling effect.[16] During these processes, reagglomeration frequently gains the upper hand rather than stripping. Apart from control over the number of layers, it is also not susceptible to functionalize commercial h-BN particles owing to the inertness of the chemical reaction.[17] Among all of the different modifications, it has been verified that several novel functionalities can be added to h-BNNS by applying O doping. For instance, an O element with great electronegativity will give the substrate stronger polarity, which promotes a more stable dispersion in solution and higher adsorption capacity performance.[18] Additionally, O atoms in the h-BNNS layer can attach to a decorated catalyst particle in a unique way, inducing enhanced catalytic ability and longer cycle life.[19] Furthermore, doped O element can reduce its bandgap and modulate original electrical insularity into semiconductivity without altering the lamellar structure.[20] To the best of our knowledge, for the preparation of h-BNNS with a few number of layers, a certain amount of O element doping and high productivity are still urgently needed.[21]

In this paper, we developed an innovative two-step method by combining the benefits of both strategies listed above. We started from the synthesis of h-BN powder through pyrolysis of a B- and N-containing precursor. This provides easy access to subsequent exfoliation and also sets the stage for adjusting the O doping composition. Then we performed hydrothermal stripping to disperse the agglomerated polycrystals into discrete nanosheets. The prepared h-BNNS has an extremely thin thickness and greatly improved yield. This novel approach shows a significant advantage compared with solvent exfoliation of commercial h-BN powder and provides an alternative idea for the preparation of other 2D nanosheet materials.

2. MATERIALS AND METHODS

2.1. Materials and Preparation Methods. The following reagents with analytical purity specifications were purchased and used directly without any further purification: melamine ($C_3N_6H_6$, Sigma-Aldrich), boric acid (H_3BO_3, Aladdin), *N*,*N*-dimethylformamide (DMF, Aladdin), acetonitrile (Innochem), *n*-propanol (Innochem), cyclohexane (Innochem), ammonium fluoride (NH_4F, Sigma-Aldrich), and h-BN powder (size of 1−2 μm, Aladdin).

In a typical synthesis, $C_3N_6H_6$ and H_3BO_3 with a molar ratio of 1:2 (melamine diborate, M·2B) were added to different solvents to get a homogeneous solution with a concentration of 1 mol/L. The transparent solution was then sealed in a Teflon-lined stainless steel autoclave and heated at 150 °C for 24 h for complete dissolution. After naturally cooling to room temperature, the precursor recrystallized followed by subsequent filtration and washing. The dried precursor was transferred into a crucible and then heated to 1000 °C at a rate of 5 °C/min. Then annealing in nitrogen atmosphere was carried out for 2 h. After washing and drying, white h-BN powder was obtained and denoted as "1000 °C-2h". Different reaction conditions of temperature and time were investigated. The samples are named after the corresponding reaction condition as "temperature-time". The nitridation conversion ratio of B element in precursor into h-BN material is about 50% with some inevitable sublimation. Then 1 g of h-BN powder was added to a NH_4F solution, sealed in a reactor with a Teflon liner, and kept at 120 °C for 30 h. The suspension was filtered and redispersed in DMF solvent following centrifugation at 1000 rpm for 30 min. The h-BNNS (denoted as "s-BNNS") collected after freeze-drying from the supernatant weighs about 35% of starting h-BN powder.

To make a comparison, an ultrasound-assisted liquid-phase stripping of commercial h-BN powder was also conducted. In a typical experiment, h-BN powder was dispersed in DMF solvent with a concentration of 1 mg/mL and stirred vigorously for 3 h. Then the suspension was treated continuously for 12 h with sonication and centrifugated at 12000 rpm for 30 min. The stripped h-BNNS (denoted as "e-BNNS") could be collected after freeze-drying the supernatant.

2.2. Characterization Methods. The crystal structure was investigated by XRD measurement with Cu Kα radiation, using a 9 kW Intelligent X-ray diffraction system provided by Smart Lab-Rigaku. The morphology was analyzed by a 200 kV field emission high-resolution transmission electron microscope (FE-HRTEM, JEOL-2100F) and scanning electron microscope (SEM, Hitachi 5-4800) using the secondary electron mode. A Nicolet iS50 model Fourier transform infrared (FTIR) spectrometer manufactured by Thermo Fisher Scientific was selected to perform scans over a wavenumber range of 400−4000 cm^{-1} to analyze the chemical bonding type. Raman spectra were measured at a power of 150 mW using DXR3 equipment produced by Thermo Fisher Scientific with a 785 nm wavelength laser. An ultraviolet−visible adsorption (UV−vis) spectrometer supplied by PerkinElmer was used to confirm the composition and concentration of the dispersion in a wavelength rNGE of 200−400 nm. Zeta potential determination in ethanol dispersion was utilized to characterize surface functionalization of the nanosheet. At the same time, full spectrum and high-resolution narrow X-ray photoelectron spectra (XPS, manufactured by Thermo Fisher Scientific) were scanned with a step size of 0.05 eV to obtain quantitative chemical composition. Different bonding types were determined by the peak splitting result, which was processed by Advantage software. In addition, the overall mass ratio of O elements contained in the sample was further determined using an O5500 Nitrogen-Oxygen-Hydrogen Analyzer by converting the solid powder into carbon oxide and detecting the gas composition by infrared spectroscopy.

3. RESULTS AND DISCUSSION

3.1. Chemical Synthesis of h-BN Powder. We aimed to synthesize h-BN powder that is more accessible for further exfoliation than well-crystallized commercial h-BN. To achieve this, it is necessary to construct heterogeneous nonmetal substitution defects and control the degree of grain growth by optimizing the precursor morphology and reaction conditions.[22] $C_3N_6H_6$ and H_3BO_3 are cost-effective choices as chemical reagents that can transform into h-BN at high

https://doi.org/10.1021/acsomega.4c00979
ACS Omega 2024, 9, 37572−37584

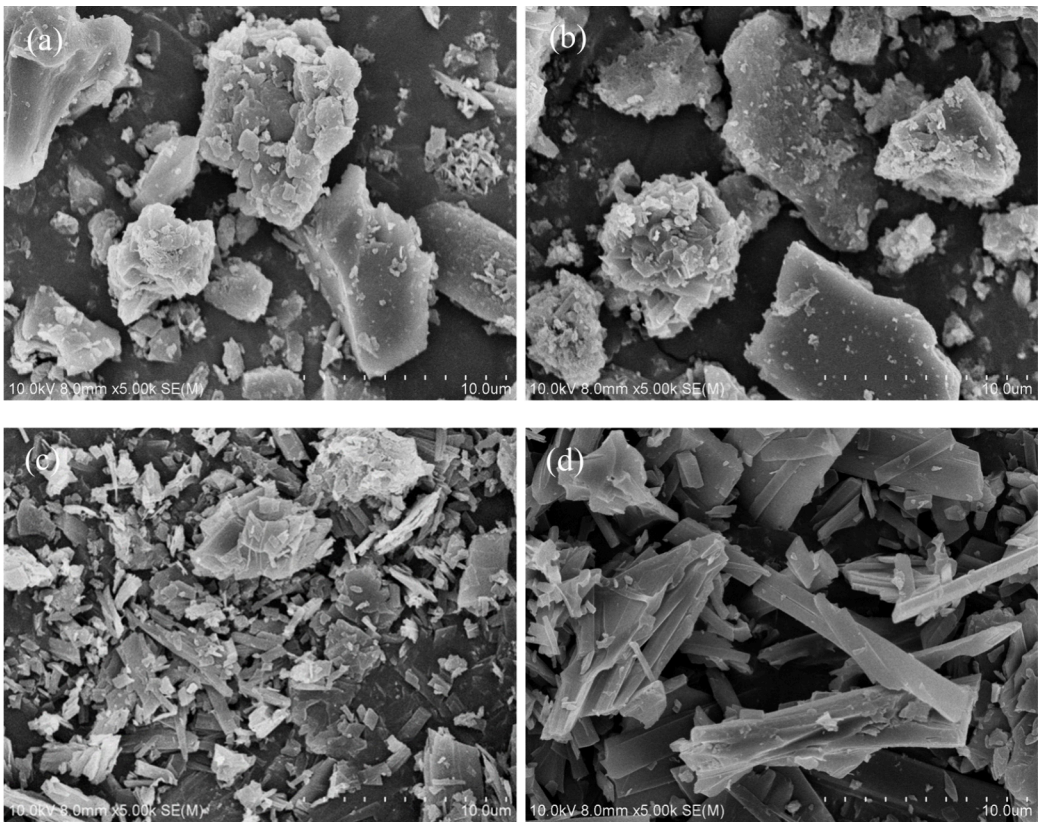

Figure 1. SEM images of M·2B precursors prepared with (a) cyclohexane, (b) *n*-propanol, (c) acetonitrile, and (d) DMF as solvents.

temperature featuring massive N and B contents. Moreover, the conversion can easily introduce C and O doping and synchronous lattice defects.[23] Usually these two ingredients are mixed together on a molecular scale by dissolving in water and recrystallizing through a drying process. However, in this way the size of the precursor is normally large, which causes the as produced h-BN powder to have a micrometer scale size as well. At the same time, the reaction is hindered from occurring at relatively low temperatures and the whole productivity is decreased. Therefore, in our research, we managed to construct a precursor with a smaller size distribution by replacing water with other solvents.

In a homogeneous solution, one $C_3N_6H_6$ molecule and two H_3BO_3 molecules can connect through hydrogen bonding between H atoms in the hydroxyl groups and N atoms in the amino groups.[24] In this way, the linked macromolecule further extends to be a ribbon-like lamellae, and many layers gradually stack on each other, forming a long-strip-like appearance.[25] The solubility of the M·2B precursor is relatively low at room temperature, and it will crystallize and precipitate upon cooling. We chose different categories of organic solvents and prepared precursors by completely dissolving and recrystallizing $C_3N_6H_6$ and H_3BO_3. The particle morphologies are shown in Figure 1 and they all exist as long and wide bundles with a rod shape which fits the typical characteristic of M·2B material. The XRD pattern shown in Figure S1 confirms the precursor composition to be a monoclinic M·2B structure. Previous research has observed that the appearance of the precursor would grow to be more obvious as the polarity of the solvent increases.[22] This is because the solute in solvent with a higher hydroxyl density can reach full dispersion and build three-dimensional attachments, which are conducive to rapid connection by hydrogen bonding during recrystallization. Our result is consistent with this study showing that the precursor becomes larger in the sequence of cyclohexane, *n*-propanol, acetonitrile, and DMF. When the precursors are collected in cyclohexane and *n*-propanol which have lower hydroxyl densities, their particle shapes shown in Figure 1a,b are relatively irregular due to the insufficient contact of $C_3N_6H_6$ and H_3BO_3 molecules. These two raw materials crystallize directly into agglomerated large particles due to the lack of spatial resistance contributed by the M·2B crystals. Only some small long strips are scattered on the particle surface, again demonstrating fewer connections through hydrogen bonding. This represents an uneven distribution of B and N sources, which is unfavorable for complete transformation into h-BN material. However, long and wide rods can be seen in the DMF-produced precursor as shown in Figure 1d, which will unfortunately result in the formation of h-BN powder with a large particle size. Owing to the structure of synthesized h-BN particles inheriting the morphology of the precursor to some extent, we consider acetonitrile to be a more suitable solvent among these four options. As given in Figure 1c, it fulfills our requirement to yield a precursor with a proper degree of cross-linking and a small particle size in the range 0.5−5 μm at the same time. By optimization of solvent components, we obtain a precursor with B and N substances blending at the molecular level and lighter particle agglomeration after recrystallization.

Then the M·2B precursor was annealed in a nitrogen atmosphere to synthesize h-BN powder. Its industrial manufacture usually requires a temperature above 1200 °C as well as a holding time of more than 5 h, which is a very energy-consuming solution. Herein, we explore the effect of diverse reaction conditions on h-BN preparation. Reaction

https://doi.org/10.1021/acsomega.4c00979
ACS Omega 2024, 9, 37572−37584

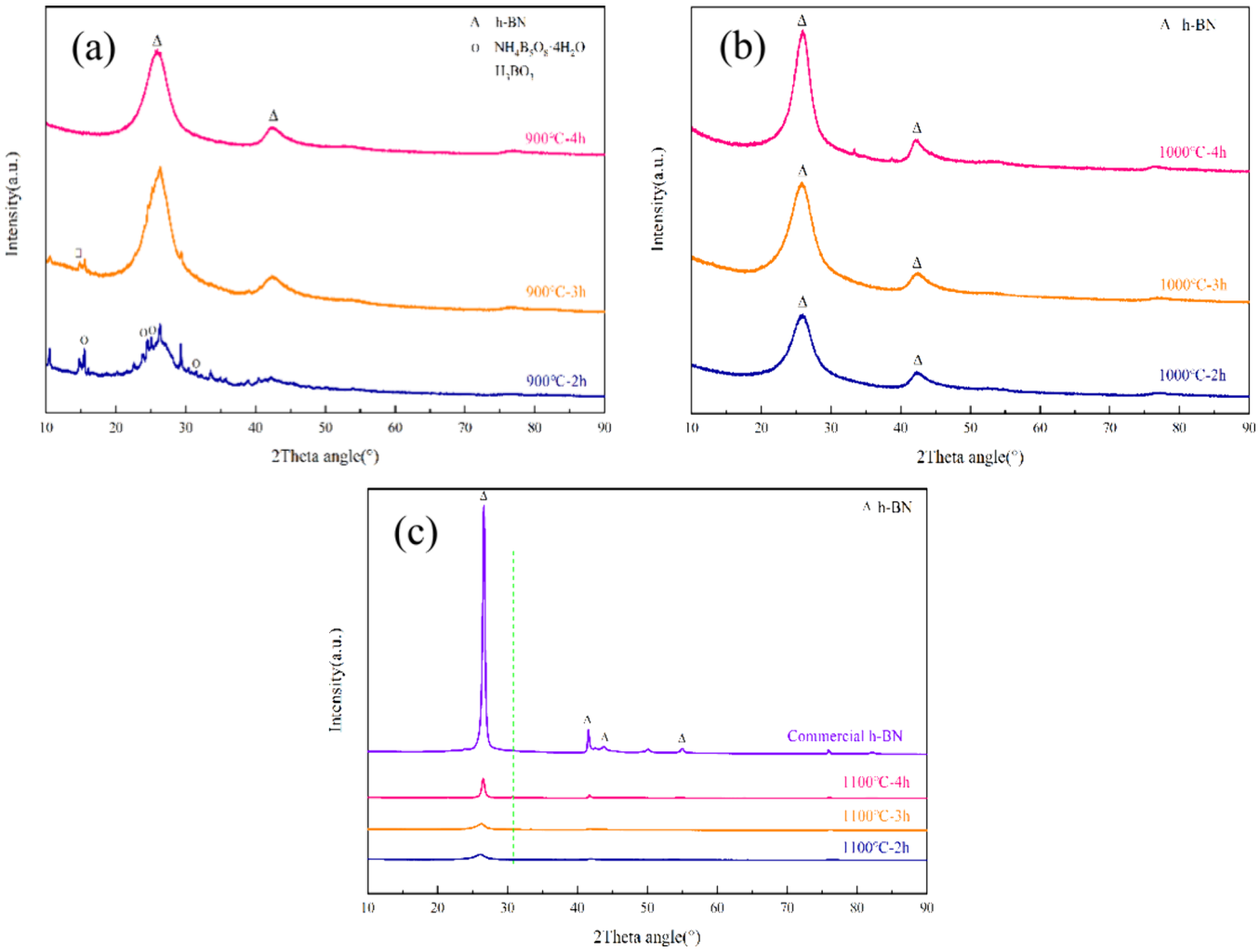

Figure 2. XRD patterns of h-BN powders synthesized at (a) 900 °C, (b) 1000 °C, and (c) 1100 °C.

Table 1. Statistics of the (002) Plane Structure of Synthetic h-BN Powders

	900 °C	1000 °C			1100 °C			
(002) plane	4h	2h	3h	4h	2h	3h	4h	commercial h-BN
2θ angle (deg)	25.959	25.965	25.972	25.995	26.200	26.360	26.540	26.820
fwhm	1.000	0.986	0.977	0.951	0.912	0.813	0.475	0.391
distance (Å)	0.343	0.343	0.343	0.342	0.340	0.338	0.336	0.332

temperature and time both have impacts on the crystal structure of the products. As given in Figure 2a, the pyrolysis reaction at 900 °C for a short time cannot fully nitrate the B source and leaves impurities like B_2O_3 and $NH_4B_5O_8·4H_2O$. Collecting a single h-BN phase requires at least 4 h. The peaks appearing at 25.9 and 42.2° are the (002) and (100) planes of the h-BN crystal, respectively. When the temperature rises to 1000 °C, we can observe that the peak intensity increases and half peak width decreases as shown in Figure 2b, which means the grain gradually becomes larger with extended heating time. At the same time, the peak position moves toward a larger angle direction, becoming nearer to the standard 2θ angle of h-BN, which implies shrinkage of the crystal cell possibly resulting from changes in elemental doping content.[26] In the meanwhile, a single phase of h-BN material and the same varying trend of peak shape appear at 1100 °C, as shown in Figure 2c. And the diffraction peak becomes a much sharper one. The average thicknesses of all h-BN powders calculated using Bragg's equation are shown in Table 1.[27] We can assume that grain growth is more sensitive to an increase in annealing temperature rather than longer holding time. For example, the calculated thickness of the (002) plane of the 1000 °C-2h sample is only one-fifth that of commercial h-BN powder. Moreover, all synthesized h-BN products, even the 1100 °C-4h sample, show a weaker crystallization degree compared with commercial h-BN powder. In order to acquire nanometer scale h-BN powder with many lattice defects which can make the subsequent exfoliation easier, we chose 1000 °C as a suitable temperature to get pure h-BN phase and an appropriate degree of grain growth.

The morphology of h-BN powders was analyzed by SEM and TEM characterization. In the inset of Figure 3a, SEM measurements at lower magnification show that synthesized powders are irregular, large particles, and most of the surface is relatively flat and smooth. When gas byproducts accumulate and then escape during the reaction procedure, a solid-phase

https://doi.org/10.1021/acsomega.4c00979
ACS Omega 2024, 9, 37572−37584

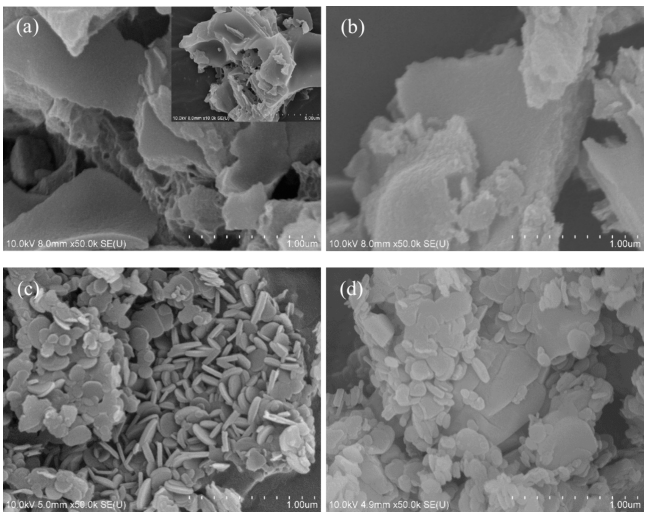

Figure 3. SEM images of h-BN powders synthesized at 1000 °C for (a) 2 h, (b) 3 h, (c) and 4 h and (d) commercial h-BN powder.

skeleton forms as the bubble's wall, which explains the genesis of this special surface shape.[28] Also there is a rough cross-section structure in which arranged protrusions represent the agglomeration of nanograins. This suggests that the transformation process is a polynuclear growth reaction of the precursor. When the reaction time is 2 h, the protruding appearance is very blurry (Figure 3a). As shown in Figure 3b, when the reaction continues to be carried out, the protrusions become more evident because the size of grains has grown to be bigger ones. When the synthesis time lasts until 4 h, we can see that multiple distinct round flakes grow together. As shown in Figure 3c, the single crystal has a diameter of about 200 nm and a thickness of about 20−50 nm, which is similar to the morphology of the smallest particles in commercial h-BN as shown in Figure 3d. However, there are also much larger powders up to 0.5−1 μm in diameter accounting for a large fraction. The effective minimization of grain size by synthesis condition control is illustrated though a comparison of h-BN particle morphology. By the way, the EDS mapping spectra (Figure S2) show that the h-BN product is mainly composed of B and N elements, while some C and O elements are evenly distributed, suggesting in situ introduced elemental doping.

We used TEM to further characterize the lamellae thickness at higher magnification, and the results are shown in Figure 4. We can see that synthesized h-BN powder is a hexagonal crystal structure based on the observation of multiple nearly rounded flakes with blurred boundaries. In addition, it is noticeable that there are many parallelly aligned lines, which implies that the copper microgrid for sample loading is perpendicular to the (002) planes of h-BN crystal (inset of Figure 4c). And the spacing between two adjacent lines is 0.35 nm, agreeing with the representative (002) plane distance.[29] Furthermore, with prolongation of the reaction time, crystal streaks appear to be more flat and ordered. The length and number of layers gradually increase, which means the crystal is becoming larger over time. By carrying a statistical calculation, the average thicknesses of h-BN products at different annealing times are 2.39, 3.53, and 6.05 nm corresponding to 7, 10, and 17 atomic layers, respectively. As shown in Figure 4d, they are apparently thinner in comparison with commercial h-BN which has a darker photo contrast and thickness ranging 20−50 nm (about 10−25 times as much as the 1000 °C-2h sample). On the basis of the above measurement, we consider that reaction at 1000 °C for 2 h is an appropriate condition for preparation of single-phase h-BN powder with fewer-numbered layers and many lattice defects. The agglomerated polycrystals can be dispersed into individual nanosheets through easier peeling than for commercial h-BN powder.

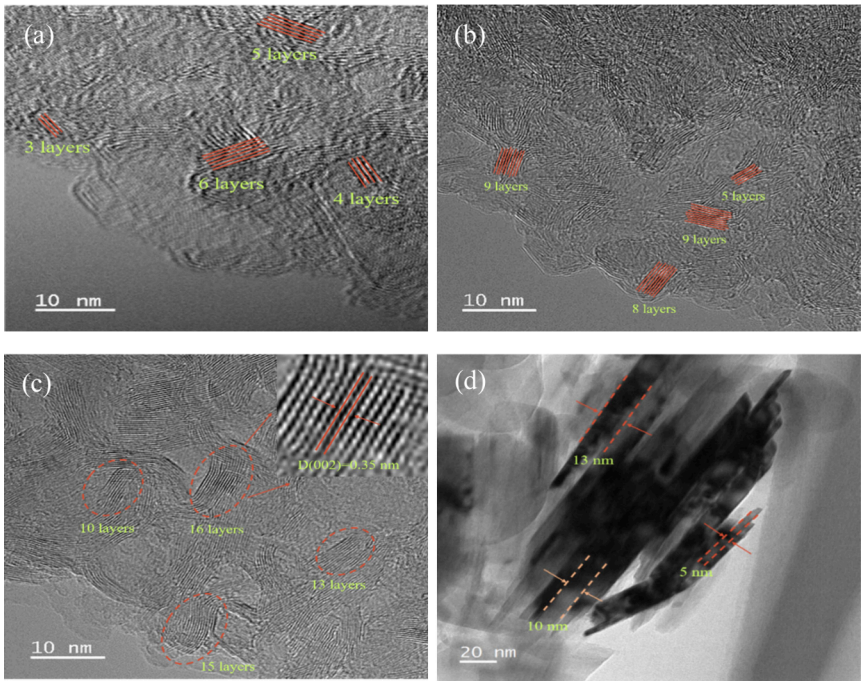

Figure 4. HR-TEM images of h-BN powders synthesized at 1000 °C for (a) 2 h, (b) 3 h, and (c) 4 h (the inset represents the enlarged (002) plane arrangement) and (d) commercial h-BN powder.

https://doi.org/10.1021/acsomega.4c00979
ACS Omega 2024, 9, 37572−37584

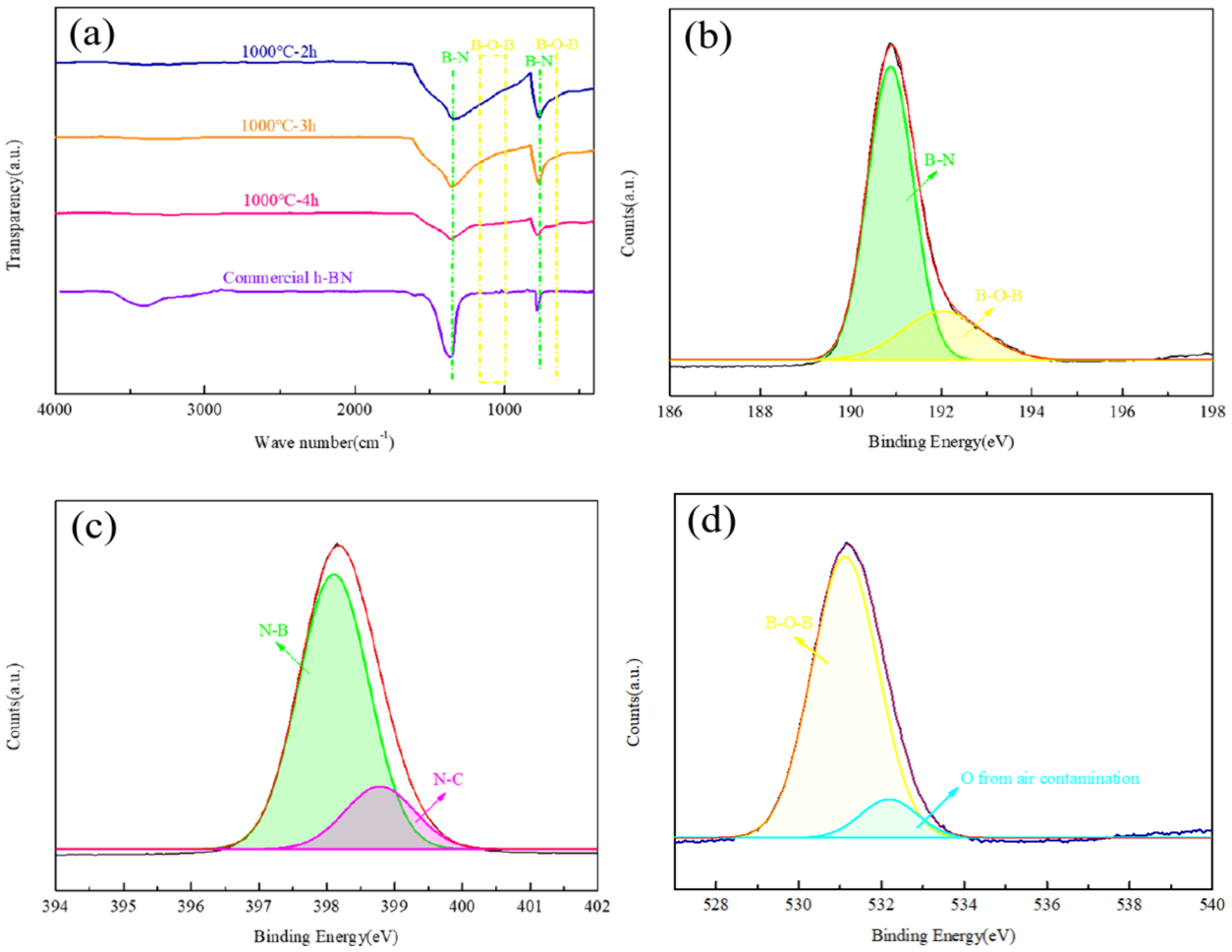

Figure 5. Surface investigation of commercial and synthetic h-BN powders: (a) FT-IR spectra of commercial h-BN powder and h-BN synthesized at 1000 °C and high-resolution XPS scanning spectra of (b) B 1s, (c) N 1s, and (d) O 1s of 1000 °C-2h h-BN powder.

The elemental composition and chemical bond type of h-BN powders prepared at 1000 °C for different calcining times are analyzed utilizing FT-IR and XPS spectra. Through the FT-IR absorbance shown in Figure 5a, we can see that absorption peaks at wavelengths of 780 and 1350 cm^{-1} show up in all the products, which represents the in-plane stretching and out-of-plane bending vibration of a B−N bond, respectively.[30] Furthermore, with prolonged reaction time, B−N peak positions undergo a red shift of about a few wavelengths toward commercial h-BN. This could be assigned to the weakened interaction of a polarizing electron cloud due to less O doping. This indicates that the synthesized powders are indeed h-BN substances, being consistent with the results of XRD analysis. Moreover, there are two additional absorption peaks appearing in the range of 1000−1170 and 656 cm^{-1} in the 1000 °C-2h sample, which cannot be found in commercial h-BN. They belong to a B−O−B bond, proving successful introduction of some O elements.[31] In the meanwhile, the broad and weak peak at a wavenumber of 3400 cm^{-1} in the spectrum of commercial h-BN is the absorption of a −OH vibration, which may be caused by surface adhesion of water in the air.[32] However, the absence of peaks at the same position in prepared h-BN powders not only indicates complete removal of surface adsorption after high-temperature synthesis but also clarifies that the edges of the nanosheet are free of −OH functionalization, which is another indistinguishable and undesirable O doping form.

In the XPS full scanning spectrum, there are four elements including B, N, O, and C existing in all the h-BN powders synthesized after different annealing times (Figure S3a). To compensate for the surface detection given by the XPS measurement, the oxygen content analysis and EDS characterization were also performed and are listed in Table 2 and Table S1, respectively. The quantitative results given by these measurements are quite similar to each other, illustrating the homogeneity of the distribution of elements on the surface and in the interior. The C concentration in the EDS result is relatively higher due to the conductive tape used for fixing the sample during the testing process, while the oxygen content

Table 2. Chemical Compositions of Commercial h-BN Powder and h-BN Synthesized at 1000 °C

	XPS investigation (atom %)				
sample	B	N	C	O	O content analysis (wt %)
1000 °C-2h	50.93	36.06	2.98	10.03	11.40
1000 °C-3h	51.02	38.87	2.43	7.68	9.27
1000 °C-4h	52.81	40.37	1.68	5.14	6.62
commercial h-BN	49.51	48.16	1.25	1.08	1.87

https://doi.org/10.1021/acsomega.4c00979
ACS Omega 2024, 9, 37572−37584

analyzer can accurately determine the mass ratio of O elements in the whole. Along with the reaction time gradually extending, the B content stays basically unchanged as about 50 atom %. At the same time, the percentage of O and C decreases, while the N content gradually increases, suggesting that the doping form may be attributed to substitutional replacement (Figure S3b). The eventual doping concentration of C is relatively small and not worthy of detailed analysis. During the heat preservation process, impurity elements, referring to C, O, and H in the precursor, can escape with gas emissions like CO_2 and H_2O, resulting in a proximate elemental ratio of B and N of nearly 1:1 in the residual h-BN material.[31] As for commercial h-BN powder, which possesses a very high analytical purity, the O element only accounts for 1.08 atom % because of the extremely intense manufacturing temperature. Moreover, such an amount of O doping is quite difficult to accomplish relying on oxidizing modification when the synthesis is accomplished due to the superior antioxidant property of the h-BN substance.

To thoroughly understand the chemical bonding of the 1000 °C-2h product, we fit the B 1s, N 1s, and O 1s high-resolution XPS spectra with a peak splitting process. In Figure 5b, we can observe that the B element has two kinds of bonds in all. The peaks appearing at the binding energy positions of 190.9 and 192.1 eV refer to B−N and B−O−B bonds, respectively.[33] While in the N 1s spectrum (Figure 5c), the peaks appearing at binding energies of 398.1 and 398.7 eV represent B−N and N−C bonds, respectively,[34] which match with the B 1s analysis. And in Figure 5d, O 1s also has a corresponding peak at 531.1 eV that is consistent with a B−O−B bond feature.[35] Based on the above results, it can be concluded that 10 atom % of O element exists in the 1000 °C-2h product as a form of the B−O−B bond, rather than an incompletely transformed H_3BO_3 residue or −OH edge functionalization. The schematic illustration of transformation from the M·2B precursor to the h-BN substance is displayed in Scheme 1. It can be determined

Scheme 1. Schematic Illustration of the Transformation from M·2B Precursor to Synthetic h-BN Powder

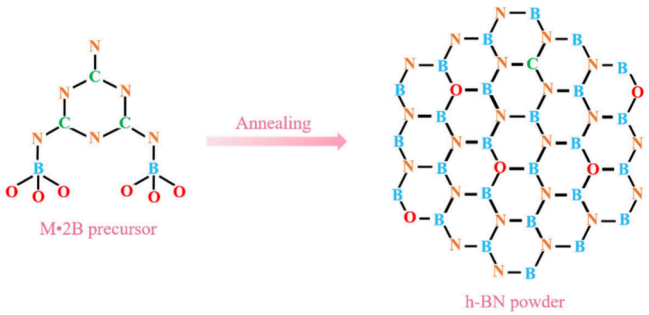

from the above results that pyrolysis can simultaneously introduce effective O element doping along with the synthesis of h-BN and the amount can be tuned in the range of 2−10 atom % by controlling the holding time (Figure S3b).

3.2. Hydrothermal Exfoliation. In summary, a precursor with small particle size was constructed at first by means of solvent optimization. Then we managed to prepare thin-layered h-BN powder with simultaneous O doping by controlling the degree of crystallization through the reaction temperature and time. Nevertheless, the polycrystalline interface of the synthesized h-BN powder needs to be dispersed, so that the acquired h-BNNS will possess a large surface area, which is favorable in many kinds of applications. For now, hydrothermal exfoliation are chosen to provide a chemical etching effect under elevated temperature and pressure circumstances. In this procedure, we select NH_4F solution as the reactant because of the chemical reactivity of F^- anions and possible intercalation impact of NH_4^+ cations.[36] Unlike liquid exfoliation with ultrasonic assistance, it does not involve significant amounts of hazardous and expensive organics. Herein, we managed to compare the h-BNNS obtained through this innovative two-step preparation method with those produced via conventional ultrasonic-assisted liquid state exfoliation. The flowchart schematics of these two means are shown in Scheme 2.

To explore whether or not the reaction product still remains as h-BN material after hydrothermal treatment, we characterized XRD and Raman measurements, and the results are shown in Figure 6. The XRD measurements in Figure 6a imply that there no impurities exist and prove that the washing treatment can totally remove all the byproducts (Figure S4). Only peaks of h-BNNS are detected. And we can see the peak undergoes a few changes in shape compared with the starting h-BN powder, like half-width widening and reduced intensity. More importantly, the peak intensity ratio of (002) to (100) plane increases from 2.97 to 5.44, which illustrates thickness reduction along the (002) plane and validates the dispersing effect of hydrothermal processing. The main peak position of synthesized 1000 °C-2h powder shifts to the left for about 0.7° after being stripped into a nanosheet.[37] Some F element addition bonded at the edge of the sheets may have caused this slight increase in layer spacing due to the electrostatic repulsion.[38] Liquid-phase stripping using commercially available h-BN also shows a similar trend in XRD patterns, which demonstrates that this divestiture also achieves a certain level of thinning in lamella thickness. Apparently, the distinct peak shape between two kinds of h-BNNS explains that there are more crystal lattice defects in s-BNNS compared with e-BNNS, which has been proven to be beneficial for gas adsorption, in situ nucleation of catalyst particle, and dispersion stability.

In Figure 6b, Raman spectra are given to further testify to the composition as well as thickness difference of h-BNNS obtained from the two preparations. The single peak appearing at 1368 cm^{-1} position represents the E_{2g} peak of h-BN material, which is caused by a stretching vibration of the B−N bond. And an additional much weaker peak occurs at 1390 cm^{-1} belonging to the A_{1g} peak, which is caused by the bending vibration of a B−N bond.[39] This result, in agreement with the above XRD analysis, indicates that the composition is still a single h-BN phase. Moreover, the peak shape of s-BNNS is not as sharp and symmetrical as that of the e-BNNS sample. It shows that the presence of element doping and crystal defects formed by controlled synthesis is more evident in the s-BNNS sample. More importantly, the red shift of the Raman peak happens at the same time, explaining the reduction of the nanosheet's thickness. For example, a shift of 4 cm^{-1} happens when the synthesized h-BN powder transforms into s-BNNS after 120 °C hydrothermal treatment. While the Raman shift position of s-BNNS appears at 1364 cm^{-1}, it was proved by a previous study that this was related to a nanosheet of less than 10 atomic layers.[40] Apparently, it can be concluded from the peak position and half-width that s-BNNS is much thinner than e-BNNS, which implies the effectiveness of preparing h-BNNS through this innovative two-step process.

https://doi.org/10.1021/acsomega.4c00979
ACS Omega 2024, 9, 37572−37584

Scheme 2. Schematic Diagrams of the Procedure Involved in the Preparation of h-BNNS Using (a) Synthesis-Dispersion Two-Step Method and (b) Liquid Phase Exfoliation Method

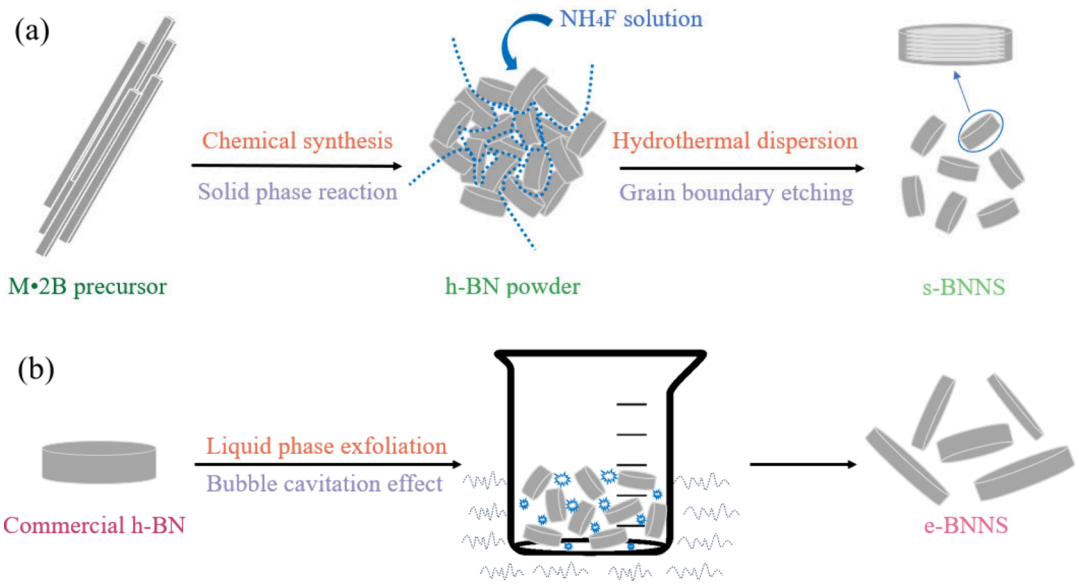

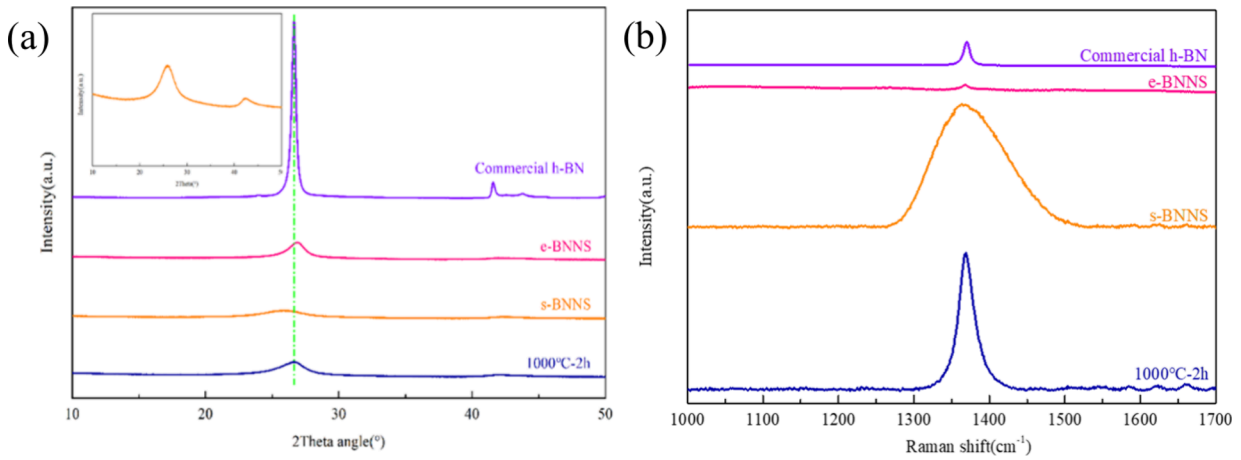

Figure 6. (a) XRD patterns (the inset shows the magnified pattern of s-BNNS) and (b) Raman characterizations of e-BNNS and s-BNNS conducted before and after stripping.

In order to further measure the elemental composition of s-BNNS, XPS characterization was performed and is given in Figure S5 and Table S2. Compared with synthetic h-BN powder, the B element in s-BNNS stays basically unchanged. The doped O concentration slightly decreases by 1.41 atom % and C by 1.15 atom % too, while the N content increases at the same time. And the F 1s spectrum inserted in Figure S5a indicates that a trace amount of F element is introduced, which should originate from the NH_4F regent. Meanwhile, the remaining O concentration in s-BNNS was further confirmed by oxygen content analyzation, which was determined to be 9.50 wt %. This displays that the chemical composition of s-BNNS is mainly controlled by the first step of the preparation referring to the synthesis of h-BN powder, and the following hydrothermal exfoliation can only alter the morphology by dispersing the polycrystalline particles into nanosheets. Based on the peak splitting results of N 1s and O 1s spectra, as given in Figure S5c,d, we can see that their chemical bonds remain the same with synthetic h-BN powder. And only a small percentage of B−F bonding appears to be a new peak in the Figure S5b, implying that F elements form a stable connection with some exposed B atoms.[36] The above results prove that the O element is successfully introduced into the prepared s-BNNS material.

In Figure 7a, the dispersion of e-BNNS exhibits an evident Tyndall effect, indicating that the particles floating in it are on the nanometer scale. However, only a light creamy suspension can be acquired using liquid phase exfoliation. As shown in Figure 7b, the s-BNNS supernatant has a milky white appearance with a significantly heavier color, implying an extraordinarily higher concentration in contrast to e-BNNS. This might be the reason its Tyndall effect pathway is not very clear. The greatly improved yield of the two-step synthesis is demonstrated by the apparent distinction in color saturation of the fluids. The e-BNNS and s-BNNS dispersions exhibit zeta potential values of -16 ± 0.38 and -39 ± 0.45 mV, respectively. The negative values reveal that both h-BNNS samples experience surface modification involving specific negatively charged functional groups. It could be inferred that some −OH connection occurs in e-BNNS. And the chemical

https://doi.org/10.1021/acsomega.4c00979
ACS Omega 2024, 9, 37572−37584

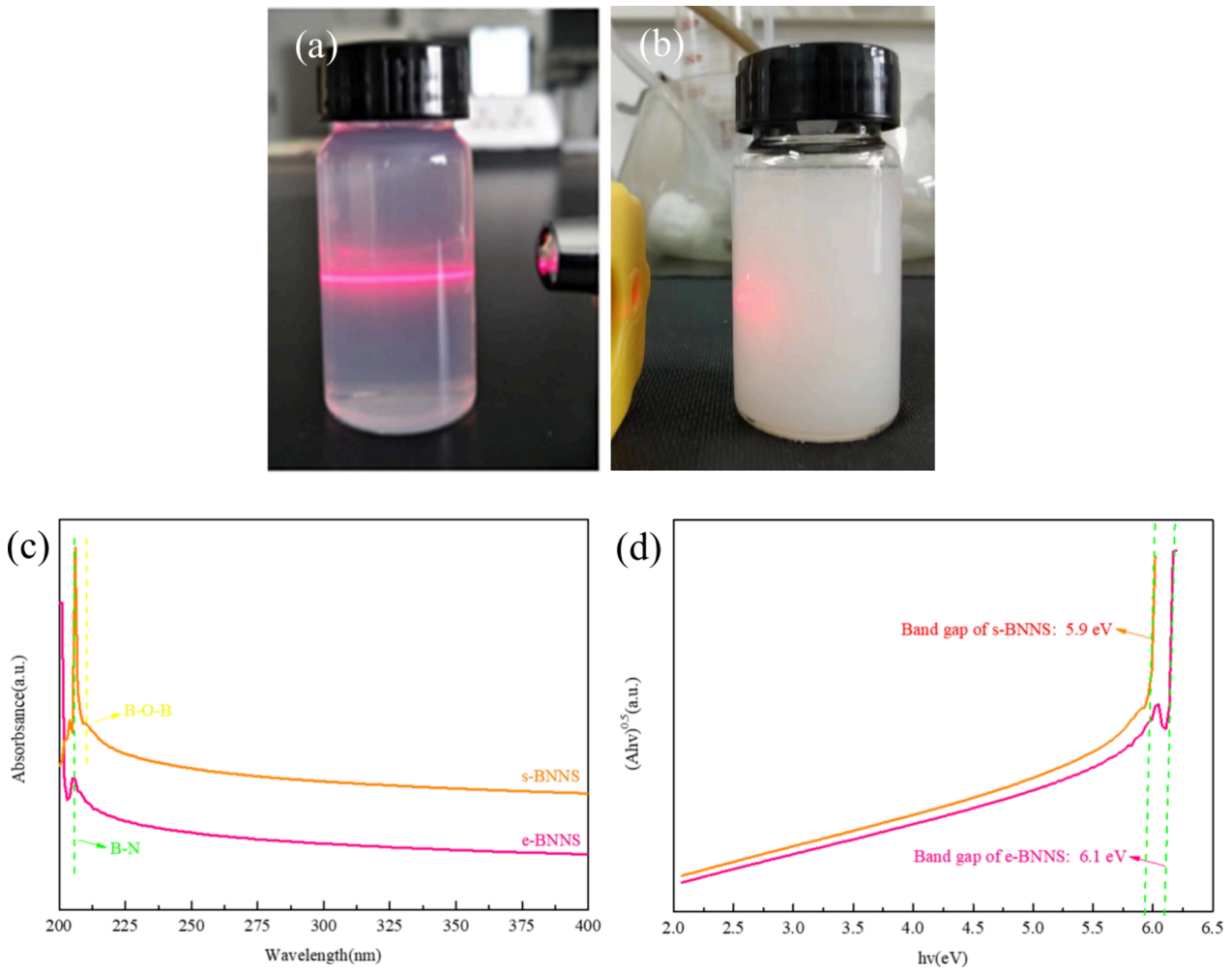

Figure 7. Photographs of (a) e-BNNS and (b) s-BNNS dispersions, (c) UV−vis absorption spectra, and (d) the corresponding Tauc plots of e-BNNS and s-BNNS.

inertness of commercial h-BN makes its participation in the reaction rather limited, which brings about a lower charge value.[41] F functionalization occurs on the surface of s-BNNS during hydrothermal stripping, as verified by combination with the aforementioned XRD observation.[16] And it has a larger zeta potential value over e-BNNS, which suggests a more stable dispersibility in ethanol.[42] Even over a 2 month period after completion of sample centrifugation, we could not see any discernible settling of the original s-BNNS dispersion.

Afterward, we analyzed the concentration of h-BNNS suspensions by UV−vis absorption spectroscopy, and the results are displayed in Figure 7c. We can observe a prominent absorption peak at 205 nm, which corresponds to the edge absorption of a B−N bond. Furthermore, s-BNNS displays another absorption peak at 212 nm, which is caused by the interaction between B and added O atoms in s-BNNS.[38] This finding aligning with the aforementioned characterizations can confirm that the two stripped products are composed of a h-BNNS phase and successful O doping in s-BNNS. Notably, the intensity of the B−N bond absorption peak in s-BNNS is almost 4 times as much as that of the e-BNNS sample, demonstrating its substantially improved concentration.[43] The result suggests a great increase in s-BNNS productivity, even within a reduced preparation time. Additionally, the Tauc plot of s-BNNS depicted in Figure 7d is derived from the UV−vis spectrum.[44] The linear extension of the plot intersects with the *X*-axis at approximately 5.9 eV, consistent with a previously reported optical band gap value.[45] No distinct peak corresponding to the doped F element has shown up, perhaps due to a small amount. Yet a decrease in band gap value of about 0.2 eV compared with e-BNNS proves its existence according to a previous study focused on the effect of F doping on h-BNNS bandwidth.[46] These examinations indicate that the s-BNNS consists of few-layered nanosheets and achieves a little extra F doping.

Then we performed TEM characterization to analyze the morphology of h-BNNS in two dispersions. Both approaches generate nanosheets with a near-circular outlined appearance. In the low-magnification view of Figure 8b and the inset picture, we are able to notice that the whole 1000 °C-2h specimen has transformed from agglomerated large particles of h-BN powder to many discrete nanosheets of s-BNNS. The distribution of lateral size falls between 10 and 20 nm, which is considerably smaller than that of e-BNNS displaying a size distribution from 50 to 100 nm. The horizontal dimensions of h-BNNS primarily originate from different raw materials prior to exfoliation because the stripping predominantly impacts their thickness. The darker color of nanosheets in Figure 8a reveals that, in comparison with s-BNNS, e-BNNS has a thicker *c*-axis scale and more uneven size distribution. In the

https://doi.org/10.1021/acsomega.4c00979
ACS Omega 2024, 9, 37572−37584

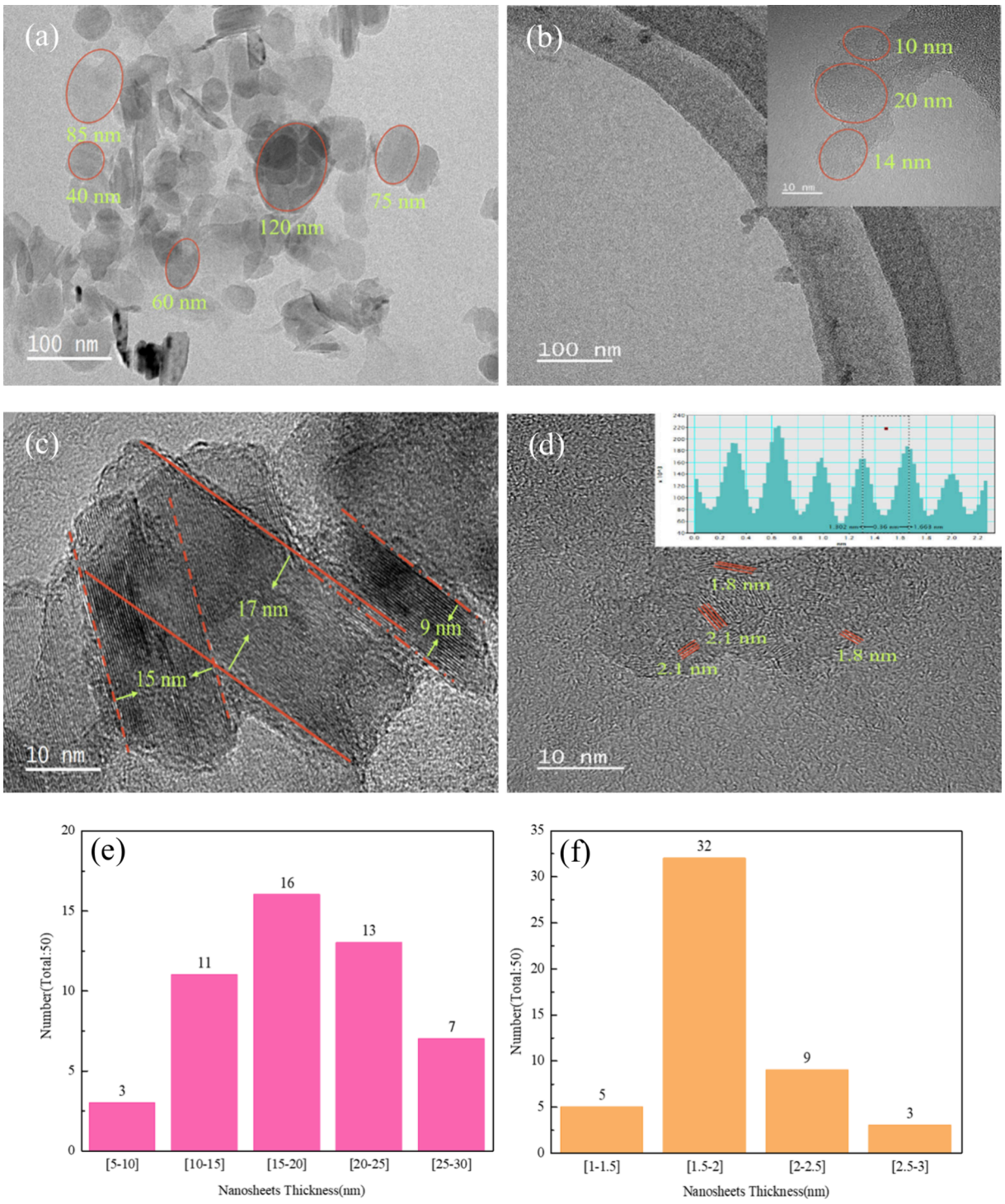

Figure 8. Low-magnification TEM images of (a) e-BNNS and (b) s-BNNS (the inset shows its TEM characterization under high magnification), HR-TEM images of (c) e-BNNS and (d) s-BNNS (the inset shows the measured distance of the (002) plane), and statistical results of nanosheet thickness distribution histograms of (e) e-BNNS and (f) s-BNNS.

high-magnification views of Figure 8c,d, we can clearly distinguish the thickness of each nanosheet. Just 6% of the nanosheets in e-BNNS possessing a thickness of less than 10 nm can be separated, even at the highest centrifugal speed of 12000 rpm. The lamellae's thickness distribution in Figure 8e is inconsistent, while the thinner layers make up a relatively small fraction of the totality. Moreover, the s-BNNS product has an approximate thickness of 1.9 nm equaling only 7 atomic layers, which are relatively near each other (Figure 8f). This exemplifies this method's capability of creating h-BNNS with a homogeneous structure and fairly small layer number. The (002) plane spacing of s-BNNS is typified by a distance of 0.36 nm between neighboring layers (inset of Figure 8d). Additionally, it slightly expanded to a greater width than for synthesized h-BN powder, which coincides with peak shifting in the XRD pattern, most likely as a result of electrostatic rejection derived from F functionalization at the margin.

https://doi.org/10.1021/acsomega.4c00979
ACS Omega 2024, 9, 37572−37584

After precursor size control and reaction condition optimization followed by hydrothermal treatment, the preparation of s-BNNS is easier to handle and has high yields compared with the complex manufacturing requirements for commercial h-BNNS product. The prepared s-BNNS has thickness at the atomic level with a uniform size distribution as well as elemental doping with adjustable contents, which benefits the reactivity of the substrate. In contrast, the commercial h-BNNS product tends to have thicker layers and extremely pure chemical composition. This combined synthesis-exfoliation preparation method opens up a new avenue for further exploration of the application of h-BNNS and other 2D materials.

4. CONCLUSIONS

In order to prepare thin-layered h-BNNS, we developed a two-step strategy involving the synthesis of h-BN powder and hydrothermal stripping. In the first step, we adjusted the particle size of the M·2B precursor and reaction conditions to generate h-BN powder with a limited degree of crystallization. Compared with commercial h-BN powder, it is more easily exfoliated into nanosheets and allows for simultaneous introduction of 10 atom % O doping. In the second step, the hydrothermal treatment transforms the polycrystalline agglomerated state into well-dispersed nanosheets. s-BNNS has diameters ranging from 10 to 20 nm and a thickness of about 7 atomic layers, which exhibits excellent dispersion stability. Compared with conventional liquid-phase exfoliation which employs commercial h-BN powder as raw material, this method makes great progress in producing nanosheets with superior uniformity in size distribution. Furthermore, our approach also achieves a higher nanosheet yield and convenient regulation over the O doping concentration. The innovative solution enables the scalable preparation of h-BNNS, which blazes the trail for academic research focusing on its integral properties and promising applications.

■ ASSOCIATED CONTENT

Supporting Information

The Supporting Information is available free of charge at https://pubs.acs.org/doi/10.1021/acsomega.4c00979.

XRD pattern of M·2B precursor, EDS mapping of synthetic 1000 °C-2h h-BN powder, chemical compositions of commercial h-BN powder and h-BN synthesized at 1000 °C, XPS full scanning and O 1s spectra of h-BN powders synthesized at 1000 °C, XRD pattern of hydrothermal product of synthetic 1000 °C-2h h-BN powder without any subsequent treatment, XPS full scanning and B 1s, N 1s, and O 1s spectra and chemical composition characterizations of s-BNNS (PDF)

■ AUTHOR INFORMATION

Corresponding Authors

Lijun Jiang − *National Engineering Research Center of Nonferrous Metals Materials and Products for New Energy, CHINA GRINM Group Co., Ltd., Beijing 100088, People's Republic of China; GRINM (Guangdong) Institute for Advanced Materials and Technology, Guangdong 528051, People's Republic of China;* orcid.org/0000-0001-8810-8697; Email: jlj@grinm.com

Wenquan Jiang − *National Engineering Research Center of Nonferrous Metals Materials and Products for New Energy, CHINA GRINM Group Co., Ltd., Beijing 100088, People's Republic of China; GRIMAT Engineering Institute Co., Ltd., Beijing 101407, People's Republic of China;* Email: jiangwenquan@grinm.com

Authors

Wenqian Li − *National Engineering Research Center of Nonferrous Metals Materials and Products for New Energy, CHINA GRINM Group Co., Ltd., Beijing 100088, People's Republic of China; GRIMAT Engineering Institute Co., Ltd., Beijing 101407, People's Republic of China; General Research Institute for Nonferrous Metals, Beijing 100088, People's Republic of China*

Yuanfang Wu − *National Engineering Research Center of Nonferrous Metals Materials and Products for New Energy, CHINA GRINM Group Co., Ltd., Beijing 100088, People's Republic of China; GRIMAT Engineering Institute Co., Ltd., Beijing 101407, People's Republic of China*

Xiumei Guo − *National Engineering Research Center of Nonferrous Metals Materials and Products for New Energy, CHINA GRINM Group Co., Ltd., Beijing 100088, People's Republic of China; GRIMAT Engineering Institute Co., Ltd., Beijing 101407, People's Republic of China*

Zhinian Li − *National Engineering Research Center of Nonferrous Metals Materials and Products for New Energy, CHINA GRINM Group Co., Ltd., Beijing 100088, People's Republic of China; GRIMAT Engineering Institute Co., Ltd., Beijing 101407, People's Republic of China*

Huiping Yuan − *National Engineering Research Center of Nonferrous Metals Materials and Products for New Energy, CHINA GRINM Group Co., Ltd., Beijing 100088, People's Republic of China; GRIMAT Engineering Institute Co., Ltd., Beijing 101407, People's Republic of China*

Man Luo − *National Engineering Research Center of Nonferrous Metals Materials and Products for New Energy, CHINA GRINM Group Co., Ltd., Beijing 100088, People's Republic of China; GRINM (Guangdong) Institute for Advanced Materials and Technology, Guangdong 528051, People's Republic of China*

Complete contact information is available at: https://pubs.acs.org/10.1021/acsomega.4c00979

Notes

The authors declare no competing financial interest.

■ ACKNOWLEDGMENTS

This work was financially sponsored by the National Key Research and Development Program of China (Grant No. 2023YFB3809103) and the National Natural Science Foundation of China (Grant No. 52271231).

■ REFERENCES

(1) Raja, I. S.; Kang, M. S.; Kim, K. S.; Jung, Y. J.; Han, D. W. Two-Dimensional Theranostic Nanomaterials in Cancer Treatment: State of the Art and Perspectives. *Cancers.* **2020**, *12*, 1657.

(2) Loske, L.; Nakagawa, K.; Yoshioka, T.; Matsuyama, H. 2D Nanocomposite Membranes: Water Purification and Fouling Mitigation. *Membranes.* **2020**, *10*, 295.

(3) Mendoza-Sánchez, B.; Gogotsi, Y. Synthesis of Two-Dimensional Materials for Capacitive Energy Storage. *Adv. Mater.* **2016**, *28*, 6104−6135.

(4) Gunjakar, J. L.; Kim, I. Y.; Lee, J. M.; Jo, Y. K.; Hwang, S. J. Exploration of Nanostructured Functional Materials Based on Hybridization of Inorganic 2D Nanosheets. *J. Phys. Chem. C* **2014**, *118*, 3847−3863.
(5) Mei, J.; Liao, T.; Kou, L.; Sun, Z. Two-Dimensional Metal Oxide Nanomaterials for Next-Generation Rechargeable Batteries. *Adv. Mater.* **2017**, *29*, 1700176.
(6) Falin, A.; Cai, Q. R.; Santos, E. J. G.; Scullion, D.; Qian, D.; Zhang, R.; Yang, Z.; Huang, S. M.; Watanabe, K.; Taniguchi, T.; Barnett, M. R.; Chen, Y.; Ruoff, R. S.; Li, H. L. Mechanical Properties of Atomically Thin Boron Nitride and the Role of Interlayer Interactions. *Nat. Commun.* **2017**, *8*, 15815.
(7) Cai, Q.; Scullion, D.; Gan, W.; Falin, A.; Zhang, S.; Watanabe, K.; Taniguchi, T.; Chen, Y.; Santos, E. J. G.; Li, L. H. High Thermal Conductivity of High-Quality Monolayer Boron Nitride and Its Thermal Expansion. *Science Advances* **2019**, *5*, eaav0129.
(8) Xue, Y. F.; Liu, Q.; He, G. J.; Xu, K. B.; Jiang, L.; Hu, X. H.; Hu, J. Q. Excellent Electrical Conductivity of the Exfoliated and Fluorinated Hexagonal Boron Nitride Nanosheets. *Nanoscale Research Letters.* **2013**, *8*, 49.
(9) Dou, H. Z.; Jiang, B.; Xu, M.; Zhang, Z.; Wen, G. B.; Peng, F. F.; Yu, A. P.; Bai, Z. Y.; Sun, Y. L.; Zhang, L. H.; Jiang, Z. Y.; Chen, Z. W. Boron Nitride Membranes with a Distinct Nanoconfinement Effect for Efficient Ethylene/Ethane Separation. *Angewandte Chemie-International Edition.* **2019**, *58*, 13969−13975.
(10) Pakdel, A.; Zhi, C.; Bando, Y.; Golberg, D. Low-Dimensional Boron Nitride Nanomaterials. *Materials Today.* **2012**, *15*, 256−265.
(11) Jiang, X. F.; Weng, Q. H.; Wang, X. B.; Li, X.; Zhang, J.; Golberg, D.; Bando, Y. Recent Progress on Fabrications and Applications of Boron Nitride Nanomaterials: A Review. *Journal of Materials Science & Technology.* **2015**, *31*, 589−598.
(12) Hirata, Y.; Yoshii, K.; Yoshizato, M.; Akasaka, H.; Ohtake, N. Developing a Synthesis Process for Large-Scale H-Bn Nanosheets Using Magnetron Sputtering and Heat Annealing. *Advanced Engineering Materials.* **2023**, *25*, 2300933.
(13) Khan, M. H.; Liu, H. K.; Sun, X.; Yamauchi, Y.; Bando, Y.; Golberg, D.; Huang, Z. Few-Atomic-Layered Hexagonal Boron Nitride: CVD Growth, Characterization, and Applications. *Materials Today.* **2017**, *20*, 611−628.
(14) Wang, X.; Zhi, C.; Li, L.; Zeng, H.; Li, C.; Mitome, M.; Golberg, D.; Bando, Y. Chemical Blowing" of Thin-Walled Bubbles: High-Throughput Fabrication of Large-Area, Few-Layered BN and C_x-BN Nanosheets. *Adv. Mater.* **2011**, *23*, 4072−4076.
(15) Angizi, S.; Alem, S. A. A.; Hasanzadeh Azar, M.; Shayeganfar, F.; Manning, M. I.; Hatamie, A.; Pakdel, A.; Simchi, A. A Comprehensive Review on Planar Boron Nitride Nanomaterials: From 2d Nanosheets Towards 0d Quantum Dots. *Progress in Materials Science.* **2022**, *124*, 100884.
(16) Luo, W.; Wang, Y.; Hitz, E.; Lin, Y.; Yang, B.; Hu, L. Solution Processed Boron Nitride Nanosheets: Synthesis. *Assemblies and Emerging Applications. Advanced Functional Materials.* **2017**, *27*, 1701450.
(17) Li, L. H.; Cervenka, J.; Watanabe, K.; Taniguchi, T.; Chen, Y. Strong Oxidation Resistance of Atomically Thin Boron Nitride Nanosheets. *ACS Nano* **2014**, *8*, 1457−1462.
(18) Lei, W.; Zhang, H.; Wu, Y.; Zhang, B.; Liu, D.; Qin, S.; Liu, Z.; Liu, L.; Ma, Y.; Chen, Y. Oxygen-Doped Boron Nitride Nanosheets with Excellent Performance in Hydrogen Storage. *Nano Energy.* **2014**, *6*, 219−224.
(19) Li, Q.; Wang, X.; Xie, Z.; Peng, X.; Guo, L.; Yu, X.; Yang, X.; Lu, Z.; Zhang, X.; Li, L. Polar Bonds Induced Strong Pd-Support Electronic Interaction Drives Remarkably Enhanced Oxygen Reduction Activity and Stability. *Applied Catalysis B: Environmental.* **2022**, *305*, 121020.
(20) Wu, M.; Yang, L.; Zhou, Y.; Jiang, J.; Zhang, L.; Rao, T.; Yang, P.; Liu, B.; Liao, W. Batio$_3$-Assisted Exfoliation of Boron Nitride Nanosheets for High-Temperature Energy Storage Dielectrics and Thermal Management. *Chemical Engineering Journal.* **2022**, *427*, 131860.
(21) Liu, Z.; Dibaji, A.; Li, D.; Mateti, S.; Liu, J.; Yan, F.; Barrow, C. J.; Chen, Y.; Ariga, K.; Yang, W. Challenges and Solutions in Surface Engineering and Assembly of Boron Nitride Nanosheets. *Materials Today.* **2021**, *44*, 194−210.
(22) Li, G.; Zhu, M.; Gong, W.; Du, R.; Eychmüller, A.; Li, T.; Lv, W.; Zhang, X. Boron Nitride Aerogels with Super-Flexibility Ranging from Liquid Nitrogen Temperature to 1000 °C. *Advanced Functional Materials.* **2019**, *29*, 1900188.
(23) Wu, C.; Wang, B.; Wu, N.; Han, C.; Zhang, X.; Wang, Y. In Situ Molten Phase-Assisted Self-Healing for Maintaining Fiber Morphology During Conversion from Melamine Diborate to Boron Nitride. *RSC Advances.* **2020**, *10*, 11105−11110.
(24) Roy, A.; Choudhury, A.; Rao, C. N. R. Supramolecular Hydrogen-Bonded Structure of a 1:2 Adduct of Melamine with Boric Acid. *J. Mol. Struct.* **2002**, *613*, 61−66.
(25) Zhong, J. C.; Feng, Y. C.; Wang, H. Z.; Hu, D. S. Fabrication and Characterization of Hexagonal Boron Nitride Powder by a Precursor Conversion Method. *Journal of Ceramic Processing Research.* **2013**, *14*, 269−273.
(26) Lei, G.; Qi, S.; Li, H.; Xue, Y.; Shen, L.; Zheng, X.; Wang, S.; Cao, Y.; Zhan, Y. Carbon-Doped Boron Nitride Nanosheets as an Efficient Metal-Free Catalyst for the Selective Oxidation of H_2S. *Phys. Chem. Chem. Phys.* **2023**, *25*, 32317−32322.
(27) Zhao, H. R.; Ding, J. H.; Shao, Z. Z.; Xu, B. Y.; Zhou, Q. B.; Yu, H. B. High-Quality Boron Nitride Nanosheets and Their Bioinspired Thermally Conductive Papers. *ACS Applied Materials & Interfaces.* **2019**, *11*, 37247−37255.
(28) Liu, F.; Li, S.; Yu, D.; Su, Y.; Shao, N.; Zhang, Z. Template-Free Synthesis of Oxygen-Doped Bundlelike Porous Boron Nitride for Highly Efficient Removal of Heavy Metals from Wastewater. *ACS Sustainable Chemistry & Engineering.* **2018**, *6*, 16011−16020.
(29) Lei, W.; Portehault, D.; Liu, D.; Qin, S.; Chen, Y. Porous Boron Nitride Nanosheets for Effective Water Cleaning. *Nature Communications.* **2013**, *4*, 1777.
(30) Weng, Q. H.; Kvashnin, D. G.; Wang, X.; Cretu, O.; Yang, Y. J.; Zhou, M.; Zhang, C.; Tang, D. M.; Sorokin, P. B.; Bando, Y.; Golberg, D. Tuning of the Optical, Electronic, and Magnetic Properties of Boron Nitride Nanosheets with Oxygen Doping and Functionalization. *Adv. Mater.* **2017**, *29*, 1700695.
(31) L'Hermitte, A.; Dawson, D. M.; Ferrer, P.; Roy, K.; Held, G.; Tian, T.; Ashbrook, S. E.; Petit, C. Formation Mechanism and Porosity Development in Porous Boron Nitride. *J. Phys. Chem. C* **2021**, *125*, 27429−27439.
(32) Li, J.; Lin, J.; Xu, X. W.; Zhang, X. H.; Xue, Y. M.; Mi, J.; Mo, Z. J.; Fan, Y.; Hu, L.; Yang, X. J.; Zhang, J.; Meng, F. B.; Yuan, S. D.; Tang, C. C. Porous Boron Nitride with a High Surface Area: Hydrogen Storage and Water Treatment. *Nanotechnology.* **2013**, *24*, 155603.
(33) Qu, J.; Li, Q.; Luo, C.; Cheng, J.; Hou, X. Characterization of Flake Boron Nitride Prepared from the Low Temperature Combustion Synthesized Precursor and Its Application for Dye Adsorption. *Coatings.* **2018**, *8*, 214.
(34) Ding, J. H.; Zhao, H. R.; Yu, H. B. High-Yield Synthesis of Extremely High Concentrated and Few-Layered Boron Nitride Nanosheet Dispersions. *2D Materials* **2018**, *5*, No. 045015.
(35) Weng, Q.; Wang, X.; Zhi, C.; Bando, Y.; Golberg, D. Boron Nitride Porous Microbelts for Hydrogen Storage. *ACS Nano* **2013**, *7*, 1558−1565.
(36) Venkateswarlu, G.; Madhu, D.; Rani, J. V. An Effective Performance of F-Doped Hexagonal Boron Nitride Nanosheets as Cathode Material in Magnesium Battery. *Mater. Chem. Phys.* **2019**, *226*, 356−361.
(37) Nie, X.; Li, G.; Jiang, Z.; Li, W.; Ouyang, T.; Wang, J. Co-Solvent Exfoliation of Hexagonal Boron Nitride: Effect of Raw Bulk Boron Nitride Size and Co-Solvent Composition. *Nanomaterials.* **2020**, *10*, 1035.
(38) Zhao, H.; Ding, J.; Xu, B.; Zhao, X.; Zheng, Y.; Shao, Z.; Yu, H. Green Synthesis of Graphene/Boron Nitride Composites for

https://doi.org/10.1021/acsomega.4c00979
ACS Omega 2024, 9, 37572−37584

Ultrahigh Thermally Conductive Fluids. *ACS Sustainable Chemistry & Engineering.* **2019**, *7*, 14266−14272.
(39) Xiao, F.; Naficy, S.; Casillas, G.; Khan, M. H.; Katkus, T.; Jiang, L.; Liu, H.; Li, H.; Huang, Z. Edge-Hydroxylated Boron Nitride Nanosheets as an Effective Additive to Improve the Thermal Response of Hydrogels. *Adv. Mater.* **2015**, *27*, 7196−7203.
(40) Gorbachev, R. V.; Riaz, I.; Nair, R. R.; Jalil, R.; Britnell, L.; Belle, B. D.; Hill, E. W.; Novoselov, K. S.; Watanabe, K.; Taniguchi, T.; Geim, A. K.; Blake, P. Hunting for Monolayer Boron Nitride: Optical and Raman Signatures. *Small.* **2011**, *7*, 465−468.
(41) Yu, L.; Yap, P. L.; Tran, D. N. H.; Santos, A. M. C.; Losic, D. High-Yield Preparation of Edge-Functionalized and Water Dispersible Few-Layers of Hexagonal Boron Nitride (hBN) by Direct Wet Chemical Exfoliation. *Nanotechnology.* **2021**, *32*, 405601.
(42) Jiang, H.; Cai, Q.; Mateti, S.; Yu, Y.; Zhi, C.; Chen, Y. Boron Nitride Nanosheet Dispersion at High Concentrations. *ACS Applied Materials & Interfaces.* **2021**, *13*, 44751−44759.
(43) Oshina, I.; Spigulis, J. Beer−Lambert Law for Optical Tissue Diagnostics: Current State of the Art and the Main Limitations. *Journal of Biomedical Optics.* **2021**, *26*, 100901.
(44) Griffin, A.; et al. Spectroscopic Size and Thickness Metrics for Liquid-Exfoliated H-BN. *Chem. Mater.* **2018**, *30*, 1998−2005.
(45) Chen, C.; Shao, C.; Wang, A. Chemical Exfoliating of Boron Nitride into Edge-Hydroxylated Nanosheets. *J. Mater. Sci.* **2023**, *58*, 4416−4427.
(46) Fan, X.; Gan, C.; Feng, P.; Ma, X.; Yue, Z.; Li, H.; Li, W.; Zhu, M. Controllable Preparation of Fluorinated Boron Nitride Nanosheets for Excellent Tribological Behaviors. *Chemical Engineering Journal.* **2022**, *431*, 133482.

https://doi.org/10.1021/acsomega.4c00979
ACS Omega 2024, 9, 37572−37584